




# Heterogeneous expression of alternatively spliced lncRNA mediates vascular smooth cell plasticity

Jaimie M. Mayner<sup>a</sup>, Evan M. Masutani<sup>a</sup>, Elena Demeester<sup>b</sup>, Aditya Kumar<sup>a</sup>, Gail Macapugay<sup>c</sup>, Pranjali Beri<sup>a</sup>, Valentina Lo Sardo<sup>c</sup> , and Adam J. Engler<sup>a,d,1</sup> 

Edited by David Weitz, Harvard University, Cambridge, MA; received October 7, 2022; accepted May 13, 2023

9p21.3 locus polymorphisms have the strongest correlation with coronary artery disease, but as a noncoding locus, disease connection is enigmatic. The lncRNA *ANRIL* found in 9p21.3 may regulate vascular smooth muscle cell (VSMC) phenotype to contribute to disease risk. We observed significant heterogeneity in induced pluripotent stem cell–derived VSMCs from patients homozygous for risk versus isogenic knockout or nonrisk haplotypes. Subpopulations of risk haplotype cells exhibited variable morphology, proliferation, contraction, and adhesion. When sorted by adhesion, risk VSMCs parsed into synthetic and contractile subpopulations, i.e., weakly adherent and strongly adherent, respectively. Of note, >90% of differentially expressed genes coregulated by haplotype and adhesion and were associated with Rho GTPases, i.e., contractility. Weakly adherent subpopulations expressed more short isoforms of *ANRIL*, and when overexpressed in knockout cells, *ANRIL* suppressed adhesion, contractility, and  $\alpha$ SMA expression. These data suggest that variable lncRNA penetrance may drive mixed functional outcomes that confound pathology.

shear stress | sorting | lncRNA | adhesion | contractility

Cardiovascular diseases are the leading causes of death in the United States, of which coronary artery disease (CAD) accounts for over 370,000 deaths annually (1). Of the more than 10<sup>6</sup> single nucleotide polymorphisms (SNPs) in our genome (2–4), most SNPs are located in noncoding regions, making mechanisms through which they enhance disease risk enigmatic (5). SNPs having the strongest association with CAD are found in the noncoding 9p21.3 locus (6–8), occur with significant frequency and in linkage disequilibrium in most populations, and are associated with up to 60% increased risk (7). While prevalence and impact are now being widely studied, understanding mechanisms employed by the most common SNPs in 9p21.3, i.e., the “risk haplotype”, has been further complicated by their presence only in higher-order primates (9, 10). Mechanisms may also be cell type specific, given that clinical presentation can vary widely and affect different cell types differently (11).

Vascular smooth muscle cells (VSMCs), which are the primary cell type in the arterial wall and regulate vascular tone (12, 13), dedifferentiate and migrate into the intima in response to endothelium injury as part of plaque formation (14–16) forming the main cell type in the neointima (16, 17). The role of VSMCs in atherosclerosis has become increasingly recognized, with lineage tracing studies identifying that VSMC content in plaques has historically been underestimated and VSMCs misidentified as macrophages (16, 18). VSMCs exhibit remarkable plasticity, in which they dedifferentiate, from a quiescent, contractile phenotype, to a more proliferative and migratory synthetic phenotype (13–16, 19, 20). While environmental cues—ranging from substrate stiffness (13, 21–24) to soluble factors (16, 19, 25)—can direct VSMC phenotype, distinct VSMC subpopulations from unique developmental origins have been identified within the vessel wall and as a function of CAD (26).

Being limited typically to human models, studies examining 9p21.3 primarily have relied on population surveys, postmortem analyses, or primary cells isolated from other organ systems; these approaches preclude actively perturbing systems to validate causal relationship. Recently, however, patient-specific induced pluripotent stem cells (iPSCs) were generated with haplotypes representing patients who are homozygous for the risk allele (RR), homozygous nonrisk (NN), or whose RR was knocked out (KO) (27). With this approach, direct subpopulation comparisons, which originated from the same isogenic patient cell line, are possible and can more easily identify key pathways related to phenotypic plasticity. This approach also lends itself well to single-cell analyses, which can point to specific genomic mechanisms. Here, we observed phenotype heterogeneity in iPSC-derived VSMCs from patients homozygous for the risk haplotype, and via a functional sort based on adhesion, we could identify both weakly adherent (WA) and strongly

## Significance

Intronic polymorphisms in the lncRNA *ANRIL* are associated with the highest increased risk of vascular disease. Splice variants containing a proximal termination of transcription (in exon 13) are up-regulated in the presence of risk polymorphisms and cause phenotype differences in induced pluripotent stem cell–derived vascular smooth muscle cells, but with variable penetrance. By sorting cells via physical differences, we identify subpopulations within the risk haplotype that have different morphology, contraction, adhesion, integrin, and alpha smooth muscle actin expression; when overexpressing two short splice variants of *ANRIL* in knockout cells, the phenotype reverts. These data suggest a reason why vascular disease pathology may be variable in patients despite the elevated risk caused by this lncRNA.

Author contributions: J.M.M. and A.J.E. designed research; J.M.M., E.M.M., E.D., A.K., and P.B. performed research; J.M.M. and G.M. contributed new reagents/analytic tools; J.M.M. and E.M.M. analyzed data; V.L.S. generated iPSC lines; and J.M.M., V.L.S., and A.J.E. wrote the paper.

The authors declare no competing interest.

This article is a PNAS Direct Submission.

Copyright © 2023 the Author(s). Published by PNAS. This open access article is distributed under [Creative Commons Attribution-NonCommercial-NoDerivatives License 4.0 \(CC BY-NC-ND\)](https://creativecommons.org/licenses/by-nc-nd/4.0/).

<sup>1</sup>To whom correspondence may be addressed. Email: [aengler@ucsd.edu](mailto:aengler@ucsd.edu).

This article contains supporting information online at <https://www.pnas.org/lookup/suppl/doi:10.1073/pnas.2217122120/-/DCSupplemental>.

Published June 5, 2023.

adherent (SA) subpopulations within the risk haplotype. The phenotype appears to be directly modulated by the presence of the long noncoding RNA (lncRNA) *ANRIL* (28) isoforms containing a proximal transcription termination in exon 13, suggesting that variable lncRNA penetrance could drive a range of functional outcomes that lead to complex pathology.

## Results

**Haplotype Mediates iPSC-Derived VSMC Phenotype with Patient-Specific Penetrance.** iPSCs were derived from male patients who are homozygous for the RR, determined by genotyping at rs1333049, rs2383207, and r10757278 (27) or NN. To validate effects, isogenic TALEN edited knock out (RR KO) lines were created as well. iPSCs stained positive for pluripotency makers Nanog, Sox2, and Oct4 (Fig. 1*A*) and were differentiated into VSMCs (Fig. 1*B*) using a protocol developed by Cheung et al for VSMCs (29), specifically deriving cells from the lateral plate mesoderm (30, 31) as in vivo. iPSC-VSMCs from all haplotypes stained positive for SMC makers calponin and SM22 (Fig. 1*C*); however, there were notable morphological differences comparing haplotypes, with both RRWT patient lines significantly smaller than the NN and RRKO lines. Differences between RRWT lines from two independent donors were observed, while maintaining significant alteration when compared to RRKO and NNWT (Fig. 1*C* and *D*). Given the critical role that adhesion complexes play in cell spreading and morphology, we assessed integrin transcript differences via hierarchical clustering of bulk RNA sequencing data from multiple patient and clonal lines from each haplotype (27) ([Dataset S1](#)). RRWT lines (red color-coded columns) clustered together and exhibited deficits in fibronectin and collagen binding integrins, as shown by the extracellular matrix (ECM) binding partners color coded in rows (Fig. 1*E*). We also measured integrin expression at the protein level by comparing expression of ITGA3 expression, a promiscuous integrin that binds collagen, fibronectin, and laminin, in all four haplotypes seeded on either collagen ([SI Appendix, Fig. S1A](#)), laminin ([SI Appendix, Fig. S1D](#)), or fibronectin ([SI Appendix, Fig. S1E](#)), using immunofluorescent staining ([SI Appendix, Fig. S1C](#)) and found that both RRWT patients expressed less ITGA3 than NN and RR KO haplotypes only while VSMCs were seeded on collagen. RRWT also expressed less ITGA2 ([SI Appendix, Fig. S1B](#)) when seeded on collagen. To determine whether such deficits in RRWT patients resulted in functional deficits, cell adhesion strength to collagen, which also is the primary ECM constituent of the tunica media (32, 33), was investigated using a spinning disk assay ([SI Appendix, Fig. S2](#)). Comparing the shear stress value at which 50% of the population detached, i.e.,  $\tau_{50}$ , VSMCs derived from both RR patient lines were lower than both the NN and RRKO, indicating reduced adhesion strength (Fig. 1*F*). These morphological, transcriptomic, and adhesion strength differences between haplotypes suggest that haplotype-specific changes to VSMC phenotype might impact function and CAD progression, i.e., VSMC dedifferentiation from a contractile to synthetic phenotype (13–16, 19, 20). However, phenotype plasticity may not be universally penetrant, so we next employed single-cell assays to sort cells into distinct phenotypic populations, i.e., strongly versus weakly adherent cells.

**Patient-Specific Adhesion Sorting Creates Heterogeneous but Morphologically Distinct VSMC Subpopulations.** Adhesion sorting was achieved by placing cells in a microfluidic device coated with collagen that exposed cells to acute, uniform fluidic shear stress and collected those cells that detached, i.e., the WA population,

relative to the population that remained adherent, i.e., the SA population ([SI Appendix, Fig. S3](#)). The population fraction that detached was measured from device flowthrough at a shear stress of 90 dynes/cm<sup>2</sup>, which is just below the  $\tau_{50}$  for the risk haplotype. A greater percentage of cells detached for both RRWT patient lines compared to both NN and RRKO (Fig. 1*F*), confirming that adhesion deficits in RRWT VSMCs are captured by both systems, whether population or single cell based.

To understand what cell phenotype(s) composed each population, we collected and analyzed the WA and SA populations for each haplotype at 90 dynes/cm<sup>2</sup>. As expected, RRWT patient lines had a greater percentage of WA cells than their NN or RRKO counterparts (Fig. 2*A*, *Inset*). WA cells were smaller and more circular than their SA counterparts for most haplotypes (Fig. 2*A* and *B*), i.e., at this shear, this population was generally smaller than 2,000  $\mu\text{m}^2$  (>90% of the population when it exists) with a shift to high circularity values. Smaller, more circular cells are indicative of a synthetic phenotype (19, 34), suggesting that the microfluidic device could be used to sort cells into disease-relevant subpopulations. Conversely, SA cells are on average larger and less circular for both RR patient lines, but the SA population for RRWT patient 1 has considerable overlap with the WA population, with only 65% of the WA smaller than the average cell area for the line compared to 96% for RRWT patient 2 (Fig. 2). These data suggest that there could be patient-specific sorting parameters.

To sort a more distinct WA population for RRWT patient 1, we adjusted the sort parameters to be more selective for WA cells by reducing shear stress to 30 dynes/cm<sup>2</sup>. With a smaller WA population (31% of cells; Fig. 2*C*, *Inset*), 96% of the population was smaller than the 2,000  $\mu\text{m}^2$  average unsorted cell area (Fig. 2*C*), suggesting that by using patient-specific parameters, adhesion strength can sort VSMCs into morphologically distinct subpopulations. VSMCs have been shown to become more synthetic over time while in culture (35); hence, we determined whether time in culture would impact sorting. Over ten cell passages, we noted that—while there were batch effects—there was no trend linking increasing culture time to a population shift to smaller, more circular cells for either RRWT patient line ([SI Appendix, Fig. S4](#)). While all subsequent experiments were performed using VSMCs having fewer than 10 passages, these data overall suggest that the RRWT lines have a persistent more heterogeneous adhesive phenotype and a greater presence of WA cells. This phenotype is solely due to the genetic difference of the haplotype and not altered by environmental stimuli or culture conditions.

**Adhesion Sorted Cells Exhibit Functional Differences.** Having established patient-specific parameters that can separate morphologically distinct subpopulations, we next investigated whether sorted cells also exhibited functional characteristics aligned with synthetic and contractile phenotypes. Presort RRWT cells are less contractile than the NN and RRKO lines ([SI Appendix, Fig. S5A](#)) by traction force microscopy (TFM), but after sorting RRWT patient 1 (using the patient-specific shear stress of 30 dynes/cm<sup>2</sup>), the WA subpopulation was also less contractile than SA and unsorted control (US) subpopulations (Fig. 3*A* and *B*). Substrate stiffness can influence VSMC contractility (13, 21, 23, 24), but even on 10-kPa gels, a fivefold stiffer substrate, WA cells exert less strain energy compared to SA and US cells ([SI Appendix, Fig. S5B](#)). Concurrently, alpha smooth muscle actin ( $\alpha\text{SMA}$ ) is increased in the contractile phenotype (13, 19, 25), and  $\alpha\text{SMA}$  comparisons across haplotypes showed decreased expression in RRWT patient lines compared to NN and RRKO lines for the

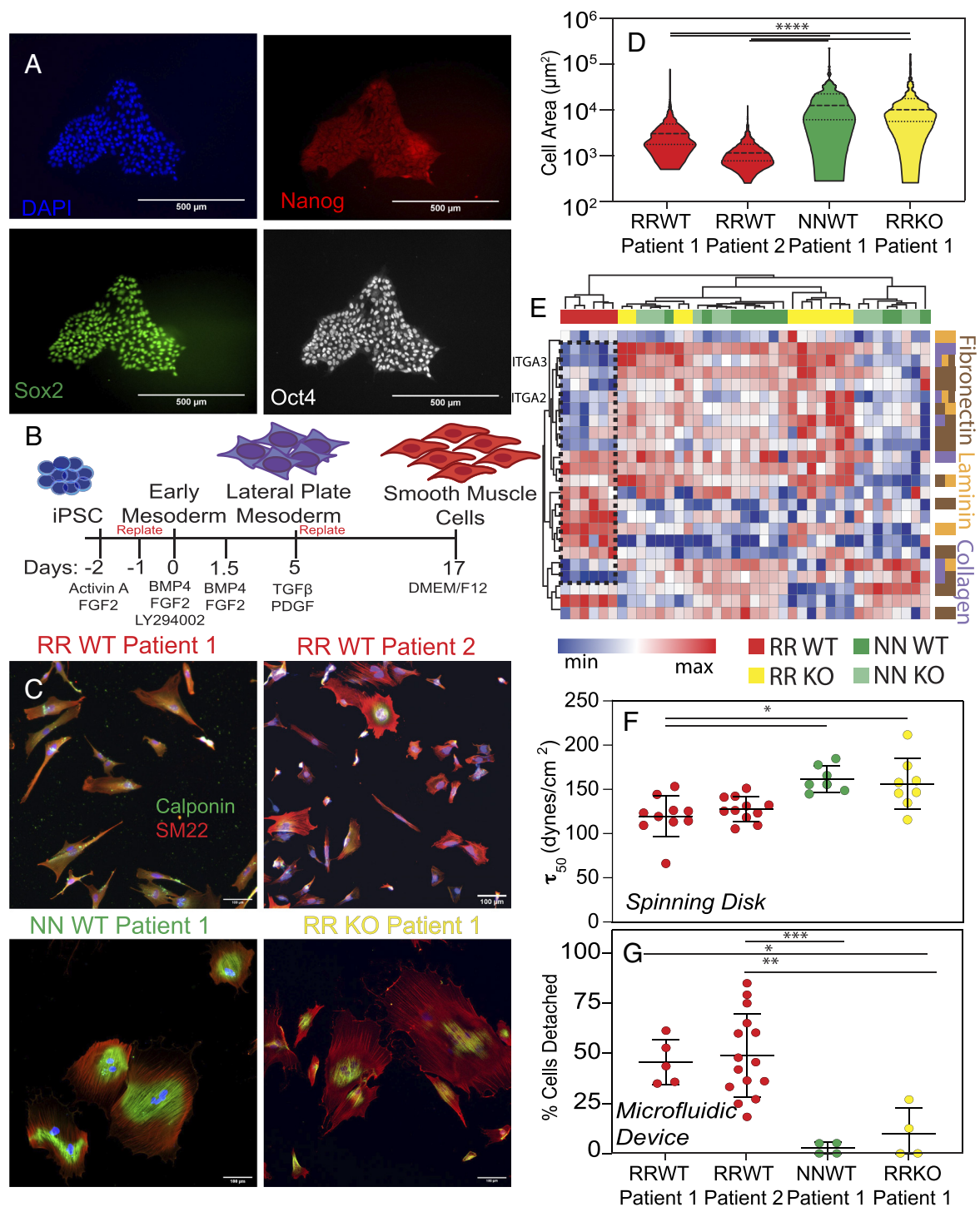


**Fig. 1.** iPSC-VSMC phenotype is haplotype mediated but has patient-specific penetrance depending on integrins. (A) Staining of patient-derived iPSCs for self-renewal markers Nanog (red), Sox2 (green), and Oct4 (white) as well as nuclei (blue). (Scale bar is 500  $\mu\text{m}$ .) (B) Schematic of differentiation process based on Cheung et al. (29). The timeline illustrates conditions, timing, and growth factors required. (C) iPSC-derived VSMCs from the indicated patient or clone with haplotype indicated by color were stained for calponin and SM22 expression. (Scale bar is 100  $\mu\text{m}$ .) (D) Cell area for the same haplotypes.  $N = 1,229, 1,286, 130$ , and  $295$  for RRWT patient 1, RRWT patient 2, NN WT patient 1, and RR KO patient 1, respectively. (E) Heatmap of integrin expression for VSMCs from the indicated haplotypes (annotated in Dataset S1), noting their extracellular matrix binding partner (at right). Hierarchical clustering of bulk RNA-seq data (27) using Euclidean distance was performed on both genes and patient samples with haplotype indicated by color; data were scaled within rows. (F) Adhesion strength, measured as the shear stress required to detach 50% of the population, i.e.,  $\tau_{50}$  (measured in dynes/cm<sup>2</sup>) using a spinning disk assay, is plotted for the indicated haplotypes.  $N = 10, 11, 7$ , and  $8$  for RR WT patient 1, RR WT patient 2, NN WT patient 1, and KO of RR patient 1, respectively. (G) Cells from the same haplotypes were also characterized for their percent detachment at  $90 \text{ dynes/cm}^2$  using a microfluidic device.  $N = 4, 15, 4$ , and  $4$  for RR WT patient 1, RR WT patient 2, NN WT, and KO of RR patient 1, respectively.  $*P < 0.05$ ,  $**P < 10^{-2}$ ,  $***P < 10^{-3}$ , and  $****P < 10^{-4}$  for one-way ANOVA with Tukey's multiple comparison test.

population (SI Appendix, Fig. S5 C and D) as well as single cells (SI Appendix, Fig. S5E). Postsort,  $\alpha\text{SMA}$  expression in the WA cell fraction of RRWT patient 1 was significantly less than SA or US control populations (Fig. 3 C and D). We also compared ITGA3 expression of the sorted populations, having found that deficits

in RRWT patient lines and integrin deficits are reported in the synthetic phenotype, and found that SA expressed significantly more ITGA3 than the WA and US (Fig. 3E). Finally, while RR patient lines proliferated significantly faster than their NN and RRKO counterparts (SI Appendix, Fig. S5F) as shown previously,



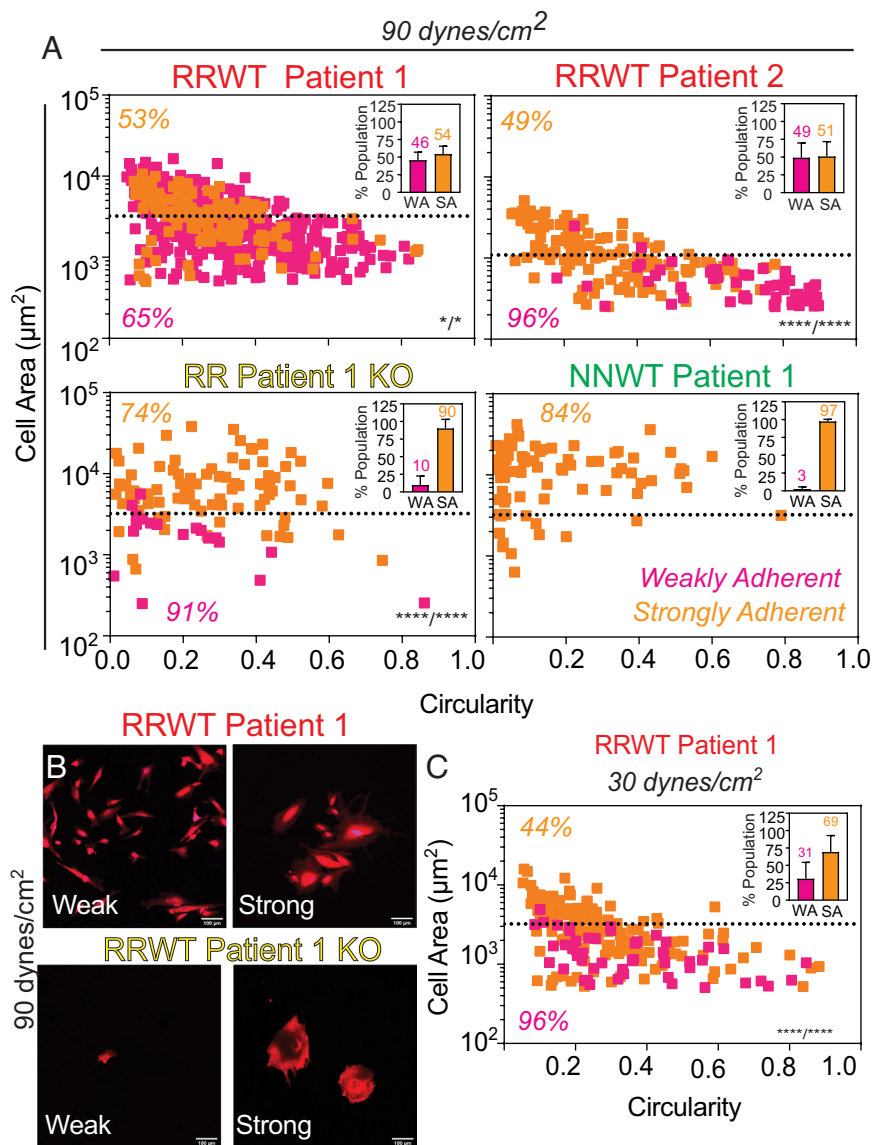


**Fig. 2.** Haplotype- and patient-specific shear-based sorting stratifies VSMC phenotype. (A) Postsort at 90 dynes/cm<sup>2</sup>, cell area and circularity measurements were plotted for weakly adherent (WA; pink) and (SA; orange) populations of the indicated haplotypes (text color coded from Fig. 1). The *Inset* bar graphs show the percentage of the population that each adhesion fraction constitutes, averaged across multiple sorts. Within the scatter plots, percentages are shown to indicate the amount of data above or below the dashed line for SA and WA cells, respectively. Note that the dashed line represents the average cell area for each haplotype. For WA cells, N = 504, 57, 22, and 0 for RR WT patient 1, RR WT patient 2, RR KO patient 1, and NN WT patient 1, respectively. For SA, N = 140, 127, 57, and 77 for RR WT patient 1, RR WT patient 2, RR KO patient 1, and NN WT patient 1, respectively. (B) Images of sorted iPSC-VSMCs (weak or strong) stained by a membrane dye. (Scale bar is 100 μm.) (C) RR WT patient 1 was sorted at 30 dynes/cm<sup>2</sup>, and area and circularity were plotted and consistent with weaker adhesion from Fig. 1 (F and G). Note that a higher percentage of WA cells are now below the dashed line because of sorting at the lower, more selective shear stress. N = 49 and 149 for WA and SA, respectively. \**P* < 0.05 and \*\*\*\**P* < 10<sup>−4</sup> for two-way ANOVA comparing haplotype area and circularity between WA and SA, with interaction and column factor comparisons, respectively.

(27) we did not find proliferation differences between our sorted population (Fig. 3F). These findings suggest that cells can be sorted by adhesion strength into populations, one of which is less contractile, expresses less contractile phenotype markers, and yet is not more proliferative. Moreover, this population is also stable and does not artificially appear due to differences in cell cycle and temporary rounding during cytokinesis.

**Differentially Expressed Genes (DEGs) Are Both Disease Relevant and Coregulated by Haplotype and Adhesion.** Underlying functional differences, we sought to understand transcriptional differences resulting from the risk haplotype and adhesion. Bulk RNA sequencing was performed on the sorted and unsorted populations from RRWT and RRKO patient 1 using multiple passages and differentiation batches. Mapped sequence run counts

were used to generate a Pearson correlation heat map for unsorted samples, which resulted in RRWT and RRKO samples from patient 1 to group together based on similarity in the whole transcriptome (SI Appendix, Fig. S6A). Three-dimensional principal component analyses (PCA) of the unsorted RRWT and RRKO transcriptome, including similar VSMC data from Lo Sardo et al (27), showed clustering by haplotype, irrespective of batch, culture time, or data source (SI Appendix, Fig. S6B). Similarly, when clustering by adhesion strength and using culture time as a covariant, 3D PCA plots show divergence of sorted cells from unsorted RRWT parental cells in opposite directions; centroids for WA and SA cells show noticeable differences in PC1 and PC3 (Fig. 4A). However, within the transcriptomes of the WA and SA cell populations, we found 2,206 DEGs—defined as a *p*-adj. value less than 0.05 (Dataset S2 and Fig. 4B). Using PANTHER to assess gene

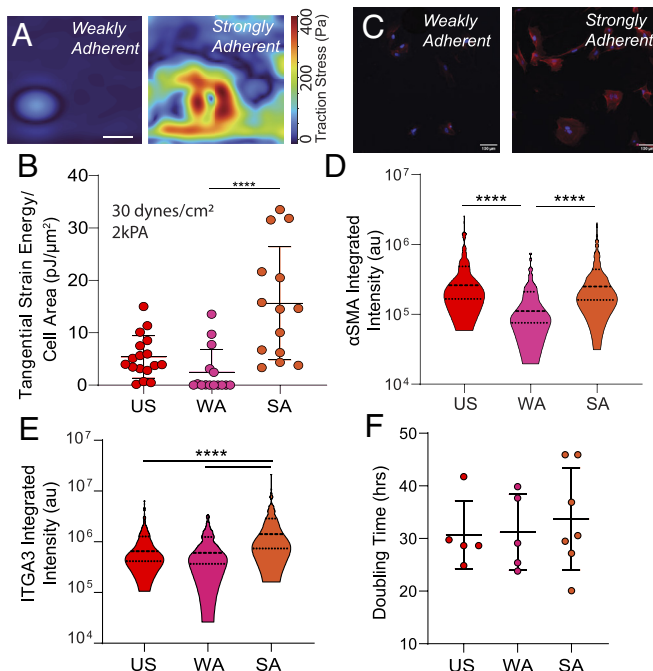


**Fig. 3.** RR WT patient 1 weakly adherent (WA) subpopulations exhibit reduced contractility and reduced contractile phenotype marker expression. (A) Heatmap displaying traction forces for a single cell measurement from traction force microscopy (TFM) performed on RR WT patient 1 VSMCs sorted at 30 dynes/cm<sup>2</sup> representative of the weakly adherent (WA) and strongly adherent (SA) populations. (Scale bar is 50 μm.) (B) Tangential strain energy normalized to cell area plotted for weakly adherent, strongly adherent, and unsorted (US) from at least three differentiation batches and sorts from RRWT patient 1. N = 17, 15, and 14 for unsorted, weakly adherent, and strongly adherent, respectively.  $^{**}P < 10^{-2}$  and  $^{\dagger}P = 0.107$  for one-way ANOVA with the Kruskal-Wallis multiple comparison test. (C) Immunofluorescence staining of alpha smooth muscle actin (αSMA) and DAPI for the sorted populations from RR WT patient 1, also over multiple differentiation batches and sorts. (Scale bar is 100 μm.) (D) αSMA expression was measured using immunofluorescence staining and measuring the integrated intensity for individual cells (au). N = 137, 114, and 294 for unsorted, weakly adherent, and strongly adherent, respectively.  $^{**}P < 10^{-2}$  and  $^{****}P < 10^{-4}$  for one-way ANOVA with Tukey's multiple comparison test. (E) ITGA3 expression was measured by immunofluorescence staining and measuring the integrated intensity for individual cells (au), with cell area identifiable by staining for DAPI and F-actin with rhodamine phalloidin. Multiple differentiation batches and sorts used. N = 220, 195, and 188 for unsorted, weakly adherent, and strongly adherent, respectively.  $^{****}P < 10^{-4}$  for one-way ANOVA with the Kruskal-Wallis multiple comparison test. (F) Doubling time (measured in hours). N = 5, 5, and 7 for unsorted, weakly adherent, and strongly adherent, respectively.

ontology (GO) enrichment for molecular function (MF) terms, several of the top 30 GO terms mapped to relevant concepts with CAD, adhesion, and the cytoskeleton (Dataset S3 and Fig. 4C). Using the same approach with haplotype comparisons, we found 693 DEGs between RRWT and RRKO (Dataset S4), and of those, 154 DEGs were common to sorted cell comparisons (Fig. 4D) for which we mapped GO terms from PANTHER (Dataset S5). Fold change for adhesion (x) and haplotype (y) were plotted against each other to determine coregulation, and we found that >90% of DEGs were coregulated with 67% being both up-regulated (Fig. 4E). Mapping the most common ontological term associated with each DEG, the most commonly coregulated genes with GO terms included regulation of cell adhesion, microtubule processing, circulatory system development, and cytoskeleton organization (Dataset S6 and Fig. 4E).

#### WA Populations Have Reduced Signaling by Rho Family GTPases and are Driven by Specific Isoforms of lncRNA ANRIL.

To identify gene pathways differentially regulated by VSMC adhesion, ingenuity pathway analysis was performed on adhesion

and haplotype DEGs. Signaling by RhoA family GTPases was a top pathway match for adhesion ( $P$  value  $< 1 \times 10^{-5}$ ) and haplotype ( $P < 0.05$ ) (Fig. 5). Thirty-one adhesion DEGs and eight haplotype DEGs mapped to the pathway, and of those, the majority showed downregulation, i.e., negative z-scores, in WA and risk haplotype-containing VSMCs. Most of these WA and/or RRWT DEGs associated with actin polymerization, contraction, proliferation, cytokinesis, and AP-1 gene-dependent expression, and this is consistent with prior GO terms, decreased adhesion, contractility, and lower αSMA expression. Data are also consistent with possibility that WA and SA cells are phenotypically distinct, with increased prevalence of WA cells in RRWT patients.

To investigate how SNPs at 9p21 could regulate RhoA signaling and result in an increased WA cell fraction, expression of ANRIL—the lncRNA which overlaps with the 9p21 locus—was measured. ANRIL is subject to posttranscriptional splicing resulting in multiple isoforms, comprising isoforms with a proximal termination of transcription in exon 13 or with a distal termination of transcription in exon 20 (SI Appendix, Fig. S7). We used a quantitative PCR method, previously described, to determine the abundance of ANRIL isoforms on our differentially adherent cells. Previously, we have reported the detection of only long isoforms A2 and A3 and short isoforms A11 and A12 in VSMCs derived from our iPSC lines (27). Long isoforms were detected by using qPCR primers spanning exons 19-20 (annotated as ANRIL 18,19 in ref. 27), while short isoforms were detected using primers binding the exon 6-7 junction. Only isoforms A2 and A3 contain exons 19-20, while A2, A11, and A12 contain the exon 6-7 junction. Risk VSMCs showed higher expression of ANRIL isoforms containing the 6-7 exon junction concomitant to equal level of isoforms containing the exon 19-20 junction. A2 and A3 (containing exons 19-20) were not detected in the RRKO, consistent with the location of TALEN-mediated deletion. Long isoforms of ANRIL containing exons 19-20 were not differentially expressed between RRWT and NN, whereas ANRIL variants containing exons 6-7 were higher in RRWT (SI Appendix, Fig. S8). These data suggest that isoforms of ANRIL containing exons 6-7 but lacking exons 19-20 (which include A11 and A12) were up-regulated in the RRWT phenotype. Next, we tested whether heterogeneous ANRIL 11 or 12 expression correlates with phenotypic heterogeneity within RRWT VSMCs, comparing expression of sorted RRWT populations. For RRWT patient 1, WA cells expressed more ANRIL containing exons 6-7 compared to both the SA and US cells, and ANRIL containing exons 19-20 long remained unchanged (Fig. 6A), again suggesting that splice variants containing exons 6-7 but not exons 19-20, which is limited to A11 and A12 in these iPSC-VSMCs, are responsible for the VSMC phenotypic change.

To determine whether the short isoforms of ANRIL, e.g., A11 or A12, were causative—and not just correlative—of phenotype plasticity, we used lentivirus to deliver A11 and A12 separately to RRKO VSMCs to determine whether it could induce an RRWT-like phenotype (SI Appendix, Fig. S9A). Across multiple differentiations and viral batches, we found that adding back A11 and A12 in a dose-dependent manner scaled directly with short ANRIL expression; rtTA and doxycycline alone—without the presence of A11 or A12 plasmids—did not increase ANRIL 6-7 expression (SI Appendix, Fig. S9B and C). Using the lowest dosage to most closely mimic ANRIL 6-7 expression levels from RRWT, we compared RRKO cells overexpressing A11 or A12, i.e., “RRKO+A11” and “RRKO+A12”, to parental cells in morphology and αSMA expression. Both RRKO+A11 and RRKO+A12 were smaller and had reduced expression of αSMA compared to RRKO (SI Appendix, Fig. S9D and E) as a direct result of the

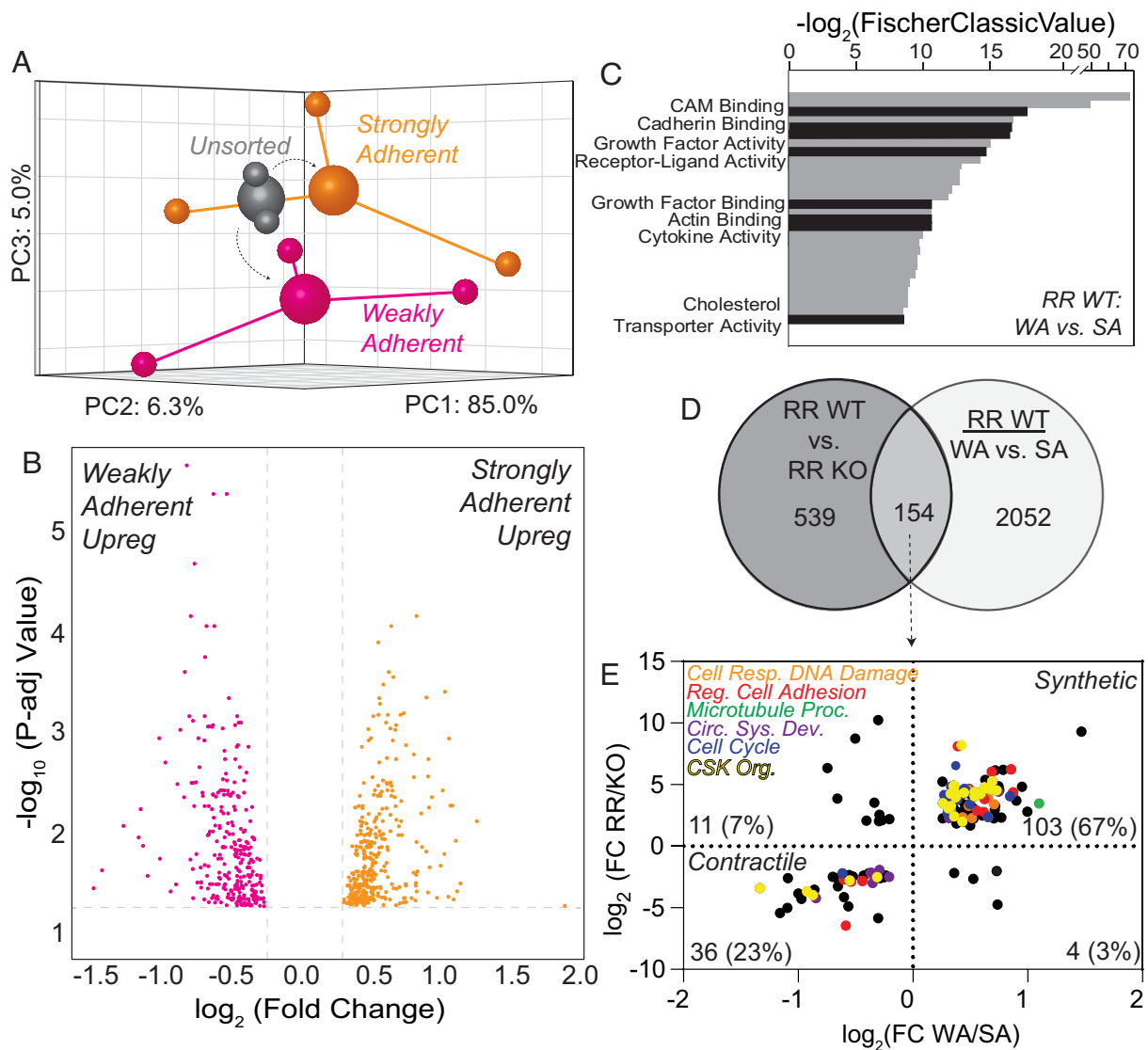


**Fig. 4.** RNA sequencing of sorted populations reveals differentially expressed genes (DEGs) that are coregulated between haplotype and adhesion. (A) RNA sequencing of RR WT patient 1 VSMC sorted populations was performed, and principal component analysis (PCA) was plotted in 3D, with the centroids for each condition shown in the color of each respective population (unsorted, weakly adherent, and strongly adherent). (B) Volcano plot of the 2,206 DEGs between weakly adherent and strongly adherent, defined as genes with  $p\text{-adj} < 0.05$ . (C) The top 30 ontological terms associated with the DEGs in B including molecular function terms, plotted using  $-\log_2(\text{Fischer Classic Value})$  and highlighting terms of interest in gray. (D) Venn diagram of DEGs for weakly adherent versus strongly adherent (light gray) and RR WT versus RR KO (dark gray), highlighting the 154 genes differentially expressed between both group comparisons. (E) DEGs common between both weakly adherent versus strongly adherent and RR WT versus RR KO were plotted based on the fold change for each comparison such that DEGs that were overexpressed in weakly adherent versus strongly adherent as well as RR WT versus RR KO were plotted in the top right quadrant (67%) and those that were overexpressed in strongly adherent versus weakly adherent and RR KO versus RR WT were plotted in the bottom left quadrant (23%). The percentage of the 154 common DEGs in each quadrant is shown, with 90% of the common DEGs coregulated color coded by associated ontological terms.

overexpression and not doxycycline treatment (*SI Appendix, Fig. S9 F and G*). In addition to size and marker expression, we sorted cells by adhesion strength to determine whether A11 and A12 shifted populations; at 90 dynes/cm<sup>2</sup> shear stress, a greater percentage of WA cells in RRKO patient 1 expressing A11 or A12 detached compared to RRKO cells cultured with or without doxycycline (Fig. 6B and *SI Appendix, Fig. S10A*). WA cells were smaller and more circular (Fig. 6B), had reduced expression of  $\alpha$ SMA (Fig. 6C), and were less contractile (Fig. 6D) than their SA counterparts for both RRKO+A11 and RRKO+A12. The WA were also less contractile than the SA and US controls, as measured by TFM for multiple sorts, differentiation and infection batches of RR KO+A11 and RR KO+A12 (Fig. 6D), further indicating that WA cells made up a different phenotype than SA cells. Notably, culturing cells in doxycycline without A11 or A12 did

not decrease cell contractility or adhesion (*SI Appendix, Fig. S10B*) as observed previously (27).

## Discussion

Genome-wide association studies have identified many disease-related SNPs; however, since many occur in noncoding loci, the mechanism(s) through which those enhance disease remains relatively unclear (2, 4, 36). SNPs at the 9p21 locus have the highest odds ratio for CAD, yet how they result in disease remains poorly understood (7–9, 37), partly due to the inadequacy of animal models, the polymorphisms occurring in linkage disequilibrium (38), overlapping risk regulators (5, 39), and the potential for bulk measurements masking important biology (40). VSMCs, which account for the majority of cells within the fibrous cap

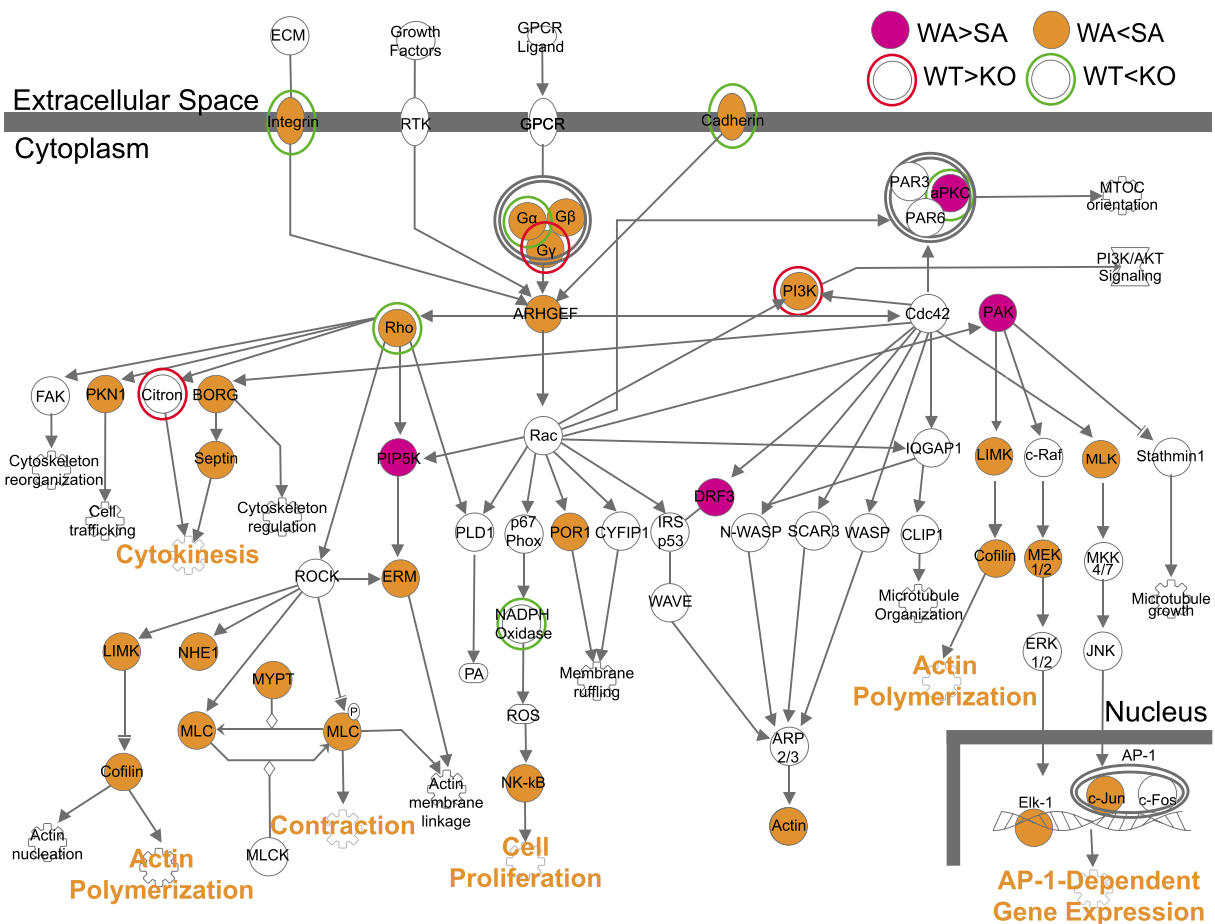


**Fig. 5.** Ingenuity pathway analysis reveals that the weakly adherent population has reduced RhoA signaling. Ingenuity pathway analysis of the genes differentially expressed between WA and SA as well as DEGs between RR WT and RR KO identified signaling by RhoA family GTPases as a top pathway. Genes overexpressed in weakly adherent compared to strongly adherent are filled with pink, whereas those overexpressed in strongly adherent are filled with orange. Those overexpressed in RR WT are circled in red, whereas those overexpressed in RR KO are circled in green.

(18), are an important cell type in atherosclerosis. As illustrated here, we used a genome editing strategy to isogenically assess variants in patient-specific, iPSC-derived VSMCs and a microfluidic approach to sort heterogeneous VSMCs into disease-relevant phenotypes. The risk haplotype increased the presence of a less adherent, less contractile phenotype within a VSMC population, but phenotype penetrance was variable; heterogeneous expression of specific isoforms of an lncRNA, which could potentially exacerbate CAD and was especially apparent when populations were sorted, could drive the variability that we observed in the lines across and within patients. Although we focused specifically on the 9p21 locus, the majority of disease-associated SNPs are in noncoding loci, and thus, it is important to recognize that some of the heterogeneity observed in disease progression (41–43) could be due to this. We believe that our findings are supportive of a general approach to exploring mechanisms by which noncoding loci enhance risk for disease and in which cellular heterogeneity is a hallmark.

It is becoming widely recognized that transcriptional differences exist even in established culture models, immortalized cell lines, or isogenic populations, and this can lead to variations in phenotype and disease penetrance. Biological markers can sort cells by function (44) but are best when used in combination (45). Here, even using a gene-edited, iPSC-based system to recapitulate disease phenotypes, we noted increased heterogeneity in morphology and cellular adhesion in the risk haplotypes consistent with variable penetrance *in vivo* (46). Unlike conventional biomarkers, our approach with a microfluidic device enables one to perform a

functional sort of cells based on their adhesion strength to ECM. While adhesion sorting is not novel, it has primarily been used to study cancer (47) or sort rare populations from blood, such as circulating tumor cells (48–50) or stem cells (51). Many diseases, including CAD, progress through the development of divergent behaviors within a cell type (41–43, 52); thus, application of biophysical sorting has the potential to unveil key insights where other methods cannot. For example, we found that adhesion-based sorting of VSMCs allowed us to isolate subpopulations of weakly and strongly adherent phenotypes and directly compare them to better assess phenotype plasticity. Many studies have assessed causes of VSMC plasticity (13, 19, 21–24), but sorting VSMCs also allowed us to establish causative links to RNA-based mechanisms and correlate them with CAD. These data also established patient-to-patient variance as well, both in phenotype plasticity and sensitivity, which is perhaps less surprising given variability in patient-derived iPSC models (53).

Not only did WA cells exhibit reduced area and increased circularity, which are morphological characteristics of synthetic VSMCs (19), but they were also less contractile than SA cells. While reduced contractility may be expected for WA cells, the correlation is not implied; previous studies of epithelial breast, prostate, and lung cancer cells did not find such a relationship (47), suggesting a cell type-specific relationship in addition to patient-to-patient variance. Other factors, e.g., morphology, height and shape, membrane rheology, focal adhesion complex turnover rate, and cell cycle, play a role in determining a cell's adhesion strength, (54) and therefore, VSMC sorting into more



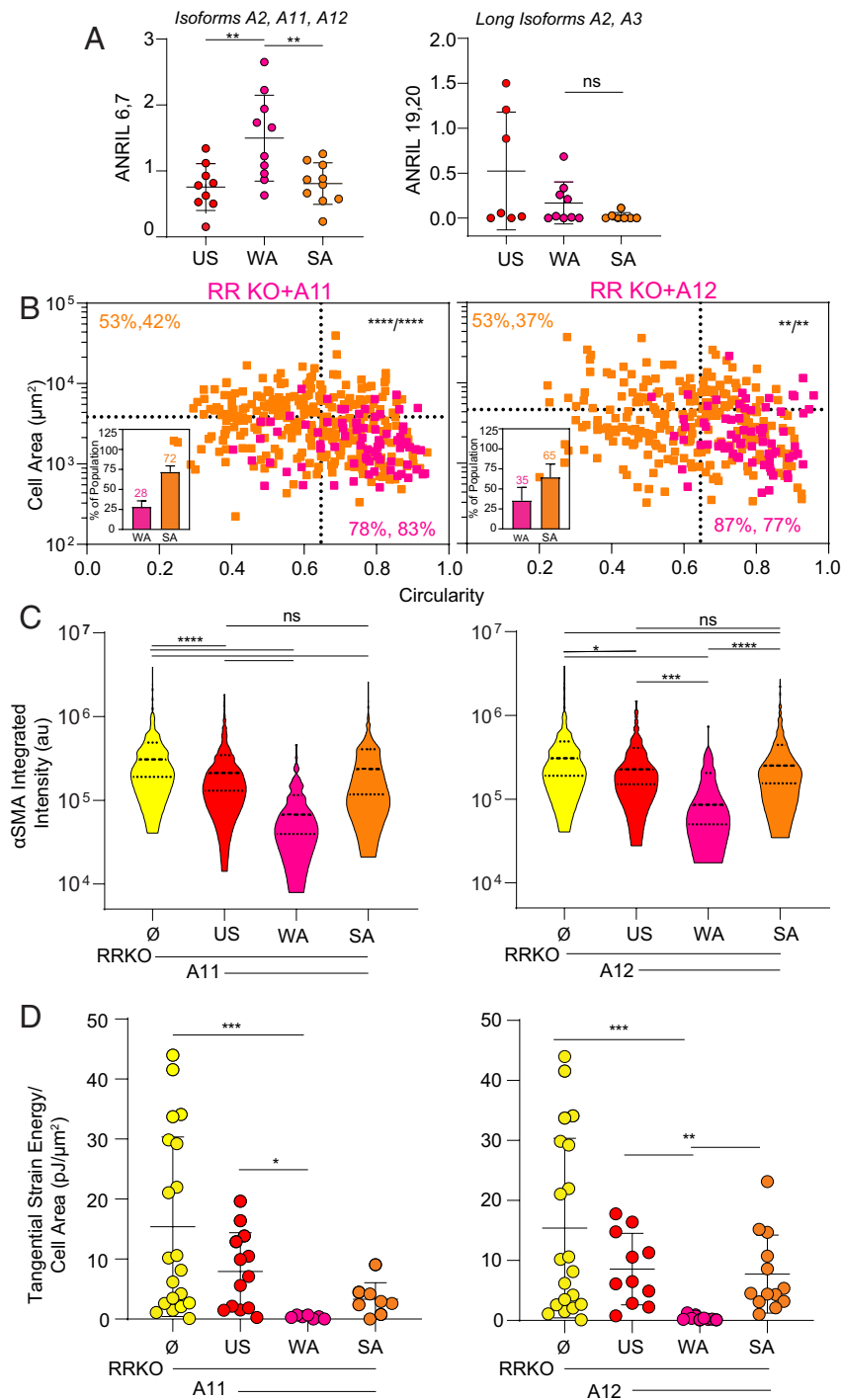


**Fig. 6.** Overexpression of A11/A12 isoforms of lncRNA ANRIL restores phenotypic heterogeneity of RR VSMCs. (A) Expression of the lncRNA ANRIL in the sorted populations (WA and SA) and unsorted (US) for RR WT patient 1 was plotted after normalization to housekeeping gene PPIA and the average expression of cells seeded in the device but not exposed to shear stress (to account for phenotypic changes from sorting). Isoforms were measured using primers binding exons 6-7 (Left; N = 9, 9, and 10 for US, WA, and SA, respectively) or exons 19-20 (right; N = 7, 10, and 7 for unsorted, weakly adherent, and strongly adherent, respectively).  $**P < 10^{-2}$  for one-way ANOVA with Tukey's multiple comparison test. (B) RR KO VSMCs overexpressing A11 (Left) and A12 (Right) were exposed to 90 dynes/ $\text{cm}^2$  of shear stress, with postsort morphology of the weakly adherent (pink) and strongly adherent (orange) populations plotted. The *Inset* bar graphs show the percentage of the population that each adhesion fraction constitutes, averaged across multiple sorts. Note that the dashed lines represent the average cell area or circularity for each respective population. Percentages shown indicate the amount of data above or below (left value) or to the right or left (right value) of the dashed lines for strongly adherent and weakly adherent cells. For A11 overexpressing cells, N = 76 and 297 for weakly adherent and strongly adherent, respectively. For A12 overexpressing, N = 70 and 242 for weakly adherent and strongly adherent, respectively.  $**P < 10^{-2}$  and  $****P < 10^{-4}$  two-way ANOVA comparing haplotype area and circularity between for weakly adherent and strongly adherent, respectively, with interaction and column factor comparisons, respectively. (C) αSMA expression was measured using immunofluorescence staining and measuring the integrated intensity for individual cells (au). N = 342, 454, 76, and 297 for null control of RR KO, A11 overexpressing unsorted, weakly adherent A11 overexpressing, and strongly adherent A11 overexpressing, respectively. N = 343, 338, 70, and 242 for null control of RR KO, A12 overexpressing unsorted, weakly adherent A12 overexpressing, and strongly adherent A12 overexpressing, respectively.  $*P < 0.05$ ,  $***P < 10^{-3}$ , and  $****P < 10^{-4}$  for one-way ANOVA with Tukey's multiple comparison test. (D) Tangential strain energy, normalized to cell area, was plotted for weakly adherent, strongly adherent, and unsorted populations from RR KO VSMCs overexpressing A11 (Left) and A12 (Right) and RR KO controls. N = 20, 13, 7, and 8 for RR KO null control, A11 overexpressing unsorted, weakly adherent, and strongly adherent, respectively, and N = 12, 9, and 13 for A12 overexpressing unsorted, weakly adherent, and strongly adherent, respectively.  $*P < 0.05$ ,  $**P < 10^{-2}$ , and  $***P < 10^{-3}$  for one-way ANOVA with the Kruskal-Wallis multiple comparison test.



and less contractile populations using adhesion strength was non-trivial. Because substrate stiffness has been shown to influence VSMC phenotype plasticity and contractility (13, 21–23), we additionally performed TFM using hydrogels of greater stiffness and found that the WA are less contractile than SA, independent of substrate stiffness. While the WA are not more proliferative than the SA, as we found the risk patient lines to be relative to the nonrisk, this indicates that the contractility differences were not artificially measured due to transient phenotypic changes that occur during cell division and that WA and SA phenotypic differences measured were independent of cell cycle status. Such trends are similar to epithelial cells (47); hence, further verification for each cell type is implied by our data contrasted with others.

As noted above, cellular heterogeneity appears linked to natural variance in lncRNA expression for ANRIL even within the same patient and haplotype, as identified by postsort population comparisons, i.e., variance was observed in only isoforms of ANRIL truncating at exon 13 and lacking exons 19, 20. While mechanical effects via adhesion differences naturally varied in the unsorted parent populations, especially for RRWT cells, it was surprising that similar variance was observed in RRKO cells artificially expressing A11 or A12 after lentiviral transformation. While virus copy number and batch effects could certainly vary between cells and data points, respectively, variance up to an order of magnitude was surprising especially when considering that RRKO cells themselves exhibited almost no variance. Although unrelated to adhesion, similar lncRNA heterogeneity in cancer can be found in and between tumors (55) and can be a predictor of distant metastasis (56); opposing adhesive behavior in epithelial carcinomas (47) versus vascular smooth muscle may also suggest that their regulation is from heterogeneous lncRNA expression. For vascular cells specifically, association studies have implicated a number of loci containing lncRNAs (6–8) to disease, with strongest association and functional regulation of VSMCs (27) found in 9p21. While here we link function to adhesion and heterogeneous expression of ANRIL, we were unable to find similar heterogeneous lncRNA regulation of vascular cells, independent of mechanics. Despite that, numerous examples exist describing lncRNAs and VSMC adhesion; the lncRNA PAXIP1-AS1 has been associated with the synthetic phenotype and reduced adhesion as observed in idiopathic pulmonary arterial hypertension (57). Conversely, the lncRNA VINAS regulates cell–cell adhesion in endothelial cells, and its silencing decreased expression of leukocyte adhesion molecules and impaired the ability of those cells to bind to the endothelium (58). While heterogeneity is not described explicitly in these systems, variance in lncRNA expression may still be present in the disease context, and our data suggest that such exploration may be warranted.

Finally, it is important to put these data in the appropriate disease context. The transcriptomic variance we observed suggests that ANRIL may have more genome-wide roles than regulating CDKN2A and CDKN2B as previously implied, and there are likely many more isoform-specific tasks than indicated here, e.g., alternatively spliced transcripts are attributed to opposing effects in endothelial cells during atherosclerosis (59). It is also not clear how SNPs drive lncRNA alternative splicing and what causes differential expression within an isogenic VSMC population. Regardless, patients with the 9p21 risk haplotype have an overabundance of VSMCs in their atherosclerotic lesions (46), and our data here suggest that this could be due to heterogeneous phenotypic switching as a result of variable expression of short isoforms of ANRIL, leading to less contractile, WA cells that heighten the risk for atherosclerotic disease. Notably, the increased heterogeneity of disease-relevant phenotypes, identifiable due to

the adhesion-based sorting strategy, could explain the incomplete penetrance of CAD by SNPs at 9p21 in patients, i.e., through incomplete penetrance of a less contractile, more synthetic WA phenotype in risk patients.

## Materials and Methods

**Ethical Compliance and Cell Lines.** The authors have complied with all ethical regulations. Human subjects were enrolled, and informed consent was obtained under a study approved by the Scripps IRB (#115676) and cells were transferred and maintained under a study approved by UCSD IRB (#141315). The lines included in this study were from three patients: C151 (NN; clone WF9), C512 (RRWT clones 1-5 and 2-3 and isogenic RR KO clones 1-9 and WB46), and C021 (RRWT clone ED2-70 and isogenic RR KO clone ED2-65). Isogenic KO lines were derived by TALEN-mediated genome editing as previously described (27).

**iPSC Maintenance and Smooth Muscle Cell Differentiation.** iPSCs were cultured on Matrigel (BioLegend) coated six-well plates in mTSE stem cell culture media (Stem Cell Technologies), with media changed daily and cells passaged using Versene (Thermo Fisher) and a cell scraper. To induce differentiation, a previously established SMC differentiation protocol (29) was followed, specifically the method for deriving SMCs from the intermediate lateral plate mesoderm. One day prior to passaging, “Day -2”, when colonies were modestly sized (70% confluency), media were changed to chemically defined media, “CDM” with 5 mg/mL bovine serum albumin, fraction V (BSA, Calbiochem), 12 ng FGF2 (Proteintech Group), and 10 ng/mL activin A (BioLegend). CDM media consisted of 1:1 IMDM [+ L-glutamine + 25 mM HEPES] (Thermo Fisher): F12 [Ham nutrient mix + L-glutamine] (Thermo Fisher) 1% (v/v) chemically defined lipid concentrate (Thermo Fisher), 0.015 mg/mL transferrin (Athens Research and Technology), 0.007 mg/mL insulin (Kerafast), and 0.004% (v/v) monothioglycerol (Sigma-Aldrich). The following day, “Day -1”, cells were passaged using Versene onto 0.1% (w/v) gelatin (porcine, type A; Sigma) coated plates into 1 mg/mL poly(vinyl alcohol) (Sigma-Aldrich) CDM, “CDM PVA”, and 12 ng/mL FGF2 and 10 ng/mL activin A. On “Day 0”, cells were induced into the mesoderm by changing media to CDM PVA with 20 ng/mL FGF2, 10 uM LY294002 (LC Laboratories), and 10 ng/mL BMP4 (HumanZyme). Thirty-six h later, on “Day 1.5”, media were changed to CDM PVA with 20 ng/mL FGF2 and 50 ng/mL BMP4. Forty-eight h later, “Day 3.5”, half of the media were replaced. Thirty-six h later, on “Day 5”, cells were split onto new gelatin-coated wells, at 190,000 cells/well, using TrypleE (Thermo Fisher), and resuspending in “Day 5” media, which constituted of CDM PVA with 10 ng/mL PDGF (BioLegend) and 2 ng/mL TGF- $\beta$  (BioLegend). Twenty-four h later, media were changed with “Day 5” media, and for the next 12 d, media were changed every two to three d using the same. When cells became confluent, they were split 1:3 using TrypleE and the same “Day 5” media. On day 18, the differentiation was complete, and media were changed to DMEM/F12 (Thermo Fisher) with 10% (v/v) fetal bovine serum (FBS, Gemini Bio-Products) 1% (v/v) penicillin-streptomycin (Gemini Bio-Products) and 0.2% (v/v) MEM nonessential amino acid concentrate 100 $\times$  (Thermo Fisher). VSMCs were cultured as such, changing media every two to three d and passaged using TrypleE 1:3 at least once before any experiments were performed or cells were frozen down for storage in liquid nitrogen (using the described DMEM/F12 media with 10% dimethyl sulfoxide (Sigma-Aldrich)).

**Microfluidic Device Channel Design and COMSOL Validation.** Microfluidic device channels were designed in AutoCAD, which was printed onto mylar film transparencies (Outputcity) using the 2D design to serve as the photomasks for photolithography. Channels were designed for simplicity of microfabrication as rectangular with a height of 150  $\mu$ m, large enough for cells to be transported through the channel in the streamline ( $h = 75 \mu$ m) but small enough to result in laminar flow with a large surface to maximize the number of cells and the throughput. Laminar flow was verified by calculating the Reynolds number, which for a rectangular channel is defined as  $Re = \frac{\rho U_o D_h}{\mu}$  with  $D_h = 2h$  for  $h \ll w$  where  $\rho$  is fluid's density,  $U_o$  is velocity,  $D_h$  is hydraulic diameter, and  $\mu$  is viscosity. The maximum flow rate, 90 ml/min, was calculated by solving for flow rate with a Reynolds number of 2,000, which results in shear stresses of 2,670 dynes/cm<sup>2</sup>, a magnitude of order larger than the shear stresses identified using the spinning disk assay to remove 50% of the cell populations. A larger surface area of 2,214 mm<sup>2</sup> is achieved using a channel with a width of 1.5 mm and turns with a

radius of curvature of 1 mm, which allow the channel to cover a large area on the 4-inch silicon wafer onto which the design is microfabricated. The 3D design was imported into COMSOL Multiphysics software, and the laminar flow physics (spf) was used to simulate fluid flow of an incompressible fluid and shear stress over the channel surface was plotted for various input flow rates using the equation  $\tau = \dot{\gamma} * \mu$ , where  $\tau$  = shear stress,  $\dot{\gamma}$  = shear rate, and  $\mu$  = viscosity, (or COMSOL as spf.mu\*spf.sr).

**Photolithography and Silicon Wafer Fabrication.** Mastermolds with channel features were microfabricated using SU-8 2,100 (MicroChem), a permanent epoxy negative photoresist in Nano3 clean room facilities. A silicon wafer (University Wafer) was cleaned with IPA, acetone, and H<sub>2</sub>O and coated with SU-8 2,100 by using the recommended spinning parameters described by Microchem for a feature height of 150  $\mu$ m. Specifically, 4 mL of SU-8 2100 was spun first at 500 rpm for 10 s, accelerated at 100 rpm/s and then at 200 rpm for 30 s, and accelerated at 300 rpm/s. Once coated, edge beads were removed, and the wafer was baked for 5 min at 65 °C and then 28 to 30 min at 95 °C or until dry. The softly baked photoresist-coated wafer was then exposed to UV while in hard contact with the photomask using a Karl Suss Mask Aligner for 23.6 s, delivering 11 mW/cm<sup>2</sup> of power and 260 mJ/cm<sup>2</sup> of energy to cure exposed regions. The wafer was baked postexposure at 65 °C for 5 min and then for 12 min at 95 °C. The uncured photoresist was then removed by washing in SU-8 developer for 15 to 17 min. Feature height was measured using a DekTak Surface Profiler, and finished wafers were coated using chemical vapor deposition with dichlorodimethylsilane (DCDMS, Arcos) overnight.

**Soft Lithography and Microfluidic Device Fabrication.** Microfluidic devices were fabricated using polydimethylsiloxane, PDMS, Sylgard 184 (Dow Chemical Company) 1:10 curing agent to silicone elastomer and cast onto the master mold wafer. Cast samples were degassed in a vacuum chamber and cured either overnight at room temperature or at 65 °C. Inlet and outlet holes were formed by using a 1-mm biopsy punch and PDMS. PDMS was cleaned with IPA, water, and scotch tape and bound to a 10.6 cm  $\times$  10.2 cm glass slide (The Gel Company) by plasma treating each surface for 30 s using an AutoGlow Plasma System (GLOW Research), with its chamber's oxygen pressure set to 0.85 Torr and radio frequency (RF) set point at 30 W. Samples were then baked for an hour at 80 °C.

**Quantification of Adhesion Strength under Uniform Shear Stress and Adhesion Sorting.** To expose cells to a uniform shear stress in the microfluidic device, the inlet is connected to a syringe pump with a programmable flow rate through a syringe (Becton Dickinson), tubing with 1/8-inch inner diameter (Fisher Scientific), polypropylene luer fixtures (Cole Parmer), and stainless steel inlet needle (Vita Needle). Bound microfluidic devices were sterilized by running 70% ethanol through the device, having autoclaved the tubing, luer locks, and needles for 15 min at 121 °C prior. The devices are then coated with gelatin for 10 min and then serum proteins for 30 min by flowing 0.1% gelatin and DMEM/F12 + 10% FBS + 0.2% amino acid concentrate + 1% P/S through the device till it coats the surface. SMCs are then seeded in the device by flowing concentrated cell suspension at 300,000 cells/mL to result in approximately 4,000 cells/cm<sup>2</sup> through the channels at 0.1 mL/min for 0.5 mL, a low enough flow rate that the resultant shear stresses are considered not physiologically relevant and using a volume large enough to coat the device. Seeded devices are then incubated overnight at 37 °C and 5% CO<sub>2</sub> to allow for cell attachment and placed in a closed petri dish to prevent media evaporation through the porous PDMS and inlet/outlet overnight.

To perform shear assays and select for the weakly and SA populations, the chosen shear stress is achieved by adjusting the input volumetric flow rate, using the following relationship between flow rate and shear stress:

$$\tau = \frac{6\mu Q}{wh^2}$$

where  $\tau$  = shear stress  $Q$  = the flow rate,  $\mu$  = viscosity of the fluid,  $w$  = width of the channel, and  $h$  = height of the channel, as measured by the DekTak. To select the WA population, 4.5 mg/mL dextrose (Fisher) in phosphate-buffered saline (Gibco) was loaded into the syringe and run over the cells for 2 min at a preselected flow rate, while the outlet flow through containing cells was collected into a conical tube. Flow through was then counted using a hemocytometer and centrifugation at 1,500 RPM for 3 min. The cells were then either replated on gelatin-coated plates at 3,000 cell/cm<sup>2</sup> for immunofluorescent analysis or resuspended in another reagent for a different biochemical assay, such as Qiazol (Qiagen) to isolate RNA for qPCR.

The SA population was then collected by enzymatic dissociation, flowing TrypLE through the device at 0.1 mL/min for 0.5 mL, enough volume to coat the surface. The device was then incubated for 4 min, or until the cells were lifted, and the SA population was then collected in a conical tube at the outlet by running 1 mL DMEM/F12 media through the device at 1 mL/min. This fraction is counted, centrifuged, and resuspended in the same media or reagent for further analysis as was done for the WA. To measure the percentage of cells that detached from the device at a given shear stress or chosen flow rate, the transparency of the device was utilized to count the number of cells in three different representative areas of the channel, drawn onto the glass bottom. The number of cells in each area was counted and averaged before exposure to shear stress and then again immediately after WA selection.

**Spinning Disk Assay.** VSMCs were seeded onto collagen-coated glass coverslips and spun using a spinning disk protocol previously described (60).

**Data, Materials, and Software Availability.** RNA-seq data have been deposited in NCBI Gene Expression Omnibus (GEO) Database ([GSE120099](https://www.ncbi.nlm.nih.gov/geo/query/acc.cgi?acc=GSE120099) (61) and [GSE211144](https://www.ncbi.nlm.nih.gov/geo/query/acc.cgi?acc=GSE211144) (62)).

**ACKNOWLEDGMENTS.** We would like to thank Dr. Kristen Jepsen of the Institute for Genomic Medicine of the University of California San Diego (UCSD) for technical assistance with sequencing, Cody Fine, Vu Nguyen, and Elsa Molina (Sanford Consortium Stem Cell and Genomic Cores) for technical expertise in flow cytometry and microscopy, Dr. Jesse Placone (UCSD) for assistance with manuscript preparation, and Dr. Jeff Hasty (UCSD) for equipment access. This work was performed in part at the San Diego Nanotechnology Infrastructure of UCSD, a member of the National Nanotechnology Coordinated Infrastructure, which is supported by the NSF (Grant ECCS-2025752). We acknowledge funding and equipment support from the NIH (R01AG045428 and R01 to A.J.E. and S100D026929 to UCSD's Institute for Genomic Medicine Genomics Center). Fellowship support was provided by the NSF (to A.K. and P.B.), NIH (T32HL105373 to J.M.M. and T32GM008666 to E.M.M.), and American Heart Association (20PRE35180166 to E.M.M.).

Author affiliations: <sup>a</sup>Chien-Lay Department of Bioengineering, University of California, San Diego, La Jolla, CA 92093; <sup>b</sup>Division of Biological Sciences, University of California, San Diego, La Jolla, CA 92093; <sup>c</sup>Department of Cell and Regenerative Biology, University of Wisconsin-Madison, Madison, WI 53705; and <sup>d</sup>Sanford Consortium for Regenerative Medicine, La Jolla, CA 92037

1. CDC, Heart disease facts & statistics | cdc.gov. <https://www.cdc.gov/heartdisease/facts.htm>. Accessed 24 May 2023.
2. E. J. Topol, J. Smith, E. F. Plow, Q. K. Wang, Genetic susceptibility to myocardial infarction and coronary artery disease. *Hum. Mol. Genet.* **15**, R117–R123 (2006).
3. R. Roberts, A. F. R. Stewart, Genes and coronary artery disease: Where are we? *J. Am. College Cardiol.* **60**, 1715–1721 (2012), [10.1016/j.jacc.2011.12.062](https://doi.org/10.1016/j.jacc.2011.12.062).
4. F. Cambien, L. Tiret, Genetics of cardiovascular diseases: From single mutations to the whole genome. *Circulation* **116**, 1714–1724 (2007).
5. M. A. Schaub, A. P. Boyle, A. Kundaje, S. Batzoglou, M. Snyder, Linking disease associations with regulatory information in the human genome. *Genome Res.* **22**, 1748–1759 (2012).
6. A. Helgadottir *et al.*, A common variant on chromosome 9p21 affects the risk of myocardial infarction. *Science* **1979**, 1491–1493 (2007).

7. N. J. Samani, H. Schunkert, Chromosome 9p21 and cardiovascular disease: The story unfolds. *Circ. Cardiovasc. Genet.* **1**, 81–84 (2008), [10.1161/CIRCGENETICS.108.832527](https://doi.org/10.1161/CIRCGENETICS.108.832527).
8. R. McPherson, Chromosome 9p21.3 locus for coronary artery disease: How little we know. *J. Am. College Cardiol.* **62**, 1382–1383 (2013), [10.1016/j.jacc.2013.07.032](https://doi.org/10.1016/j.jacc.2013.07.032).
9. R. Roberts, A. F. R. Stewart, 9p21 and the genetic revolution for coronary artery disease. *Clin. Chem.* **58**, 104–112 (2012), [10.1373/clinchem.2011.172759](https://doi.org/10.1373/clinchem.2011.172759).
10. A. Visel *et al.*, Targeted deletion of the 9p21 non-coding coronary artery disease risk interval in mice. *Nature* **464**, 409–412 (2010).
11. L. Folkersen *et al.*, Relationship between CAD risk genotype in the chromosome 9p21 locus and gene expression. Identification of eight new ANRIL splice variants. *PLoS One* **4**, e7677 (2009).
12. S. F. Louis, P. Zahradka, Vascular smooth muscle cell motility: From migration to invasion. *Exp. Clin. Cardiol.* **15**, e75–85 (2010).

13. S. Ahmed, D. T. Warren, Vascular smooth muscle cell contractile function and mechanotransduction. *Vessel Plus* **2**, 36 (2018).
14. R. Ross, The pathogenesis of atherosclerosis: A perspective for the 1990s. *Nature* **362**, 801–809 (1993).
15. R. Zargham, G. Thibault, Alpha8Beta1 Integrin expression in the rat carotid artery: Involvement in smooth muscle cell migration and neointima formation. *Cardiovasc Res.* **65**, 813–822 (2005).
16. M. R. Bennett, S. Sinha, G. K. Owens, Vascular smooth muscle cells in atherosclerosis. *Circ. Res.* **118**, 692–702 (2016).
17. T. Christen *et al.*, Mechanisms of neointima formation and remodeling in the porcine coronary artery. *Circulation* **103**, 882–888 (2001).
18. G. L. Basatemur, H. F. Jørgensen, M. C. H. Clarke, M. R. Bennett, Z. Mallat, Vascular smooth muscle cells in atherosclerosis. *Nat. Rev. Cardiol.* **16**, 727–744 (2019).
19. S. S. M. Rensen, P. A. F. M. Doevendans, G. J. J. M. van Eys, Regulation and characteristics of vascular smooth muscle cell phenotypic diversity. *Netherlands Heart J.* **15**, 100–108 (2007), 10.1007/BF03085963.
20. P. Petsofonsakul *et al.*, Role of vascular smooth muscle cell phenotypic switching and calcification in aortic aneurysm formation. *Arterioscler. Thromb. Vasc. Biol.* **39**, 1351–1368 (2019).
21. C. K. Yu, T. Xu, R. K. Assoian, D. J. Rader, Mining the stiffness-sensitive transcriptome in human vascular smooth muscle cells identifies long noncoding RNA stiffness regulators. *Arterioscler. Thromb. Vasc. Biol.* **38**, 164–173 (2018).
22. J. Qiu *et al.*, Biomechanical regulation of vascular smooth muscle cell functions: From in vitro to in vivo understanding. *J. R. Soc. Interface* **11**, 20130852 (2014), 10.1098/rsif.2013.0852.
23. S. A. Xie *et al.*, Matrix stiffness determines the phenotype of vascular smooth muscle cell in vitro and in vivo: Role of DNA methyltransferase 1. *Biomaterials* **155**, 203–216 (2018).
24. S. R. Peyton, P. D. Kim, C. M. Ghajar, D. Seliktar, A. J. Putnam, The effects of matrix stiffness and RhoA on the phenotypic plasticity of smooth muscle cells in a 3-D biosynthetic hydrogel system. *Biomaterials* **29**, 2597–2607 (2008).
25. M. R. Alexander, G. K. Owens, Epigenetic control of smooth muscle cell differentiation and phenotypic switching in vascular development and disease. *Annu. Rev. Physiol.* **74**, 13–40 (2012).
26. M. G. Frid, E. P. Moiseeva, K. R. Stenmark, Multiple phenotypically distinct smooth muscle cell populations exist in the adult and developing bovine pulmonary arterial media in vivo. *Circ. Res.* **75**, 669–681 (1994).
27. V. lo Sardo, *et al.*, Unveiling the role of the most impactful cardiovascular risk locus through haplotype editing. *Cell* **175**, 1796–1810.e20 (2018).
28. Y. Kong, C. H. Hsieh, L. C. Alonso, ANRIL: A lncRNA at the CDKN2A/B locus with roles in cancer and metabolic disease. *Front. Endocrinol. (Lausanne)* **9**, 405 (2018).
29. C. Cheung, A. S. Bernardo, R. A. Pedersen, S. Sinha, Directed differentiation of embryonic origin-specific vascular smooth muscle subtypes from human pluripotent stem cells. *Nat. Protoc.* **9**, 929–938 (2014).
30. S. Ayoubi, S. P. Sheikh, T. V. Esildsen, Human induced pluripotent stem cell-derived vascular smooth muscle cells: Differentiation and therapeutic potential. *Cardiovasc Res.* **113**, 1282–1293 (2017).
31. C. Cheung, A. S. Bernardo, M. W. B. Trotter, R. A. Pedersen, S. Sinha, Generation of human vascular smooth muscle subtypes provides insight into embryological origin-dependent disease susceptibility. *Nat. Biotechnol.* **30**, 165–173 (2012).
32. H. Mozafari, C. Zhou, L. Gu, Mechanical contribution of vascular smooth muscle cells in the tunica media of artery. *Nanotechnol. Rev.* **8**, 50–60 (2019).
33. M. K. O'Connell *et al.*, The three-dimensional micro- and nanostructure of the aortic medial lamellar unit measured using 3D confocal and electron microscopy imaging. *Matrix Biol.* **27**, 171–181 (2008).
34. S. Chang *et al.*, Phenotypic modulation of primary vascular smooth muscle cells by short-term culture on micropatterned substrate. *PLoS One* **9**, e88089 (2014).
35. S. Chang *et al.*, Phenotypic modulation of primary vascular smooth muscle cells by short-term culture on micropatterned substrate. *PLoS One* **9**, e88089 (2014).
36. R. Roberts *et al.*, Identifying genes for coronary artery disease: An idea whose time has come. *Canadian J. Cardiol.* **23**, 7A–15A (2007).
37. A. Helgadottir *et al.*, A common variant on chromosome 9p21 affects the risk of myocardial infarction. *Science* **199**, 1491–1494 (2007).
38. O. Harismendy, D. Notani, X. Song, N. G. Rahim, K. A. Frazer, 9p21 DNA variants associated with coronary artery disease impair IFN- $\gamma$  signaling response. *Nature* **470**, 264–268 (2011).
39. M. G. Larson *et al.*, Framingham heart study 100K project: Genome-wide associations for cardiovascular disease outcomes. *BMC. Med. Genet.* **8** (suppl. 1), S5 (2007).
40. S. J. Altschuler, L. F. Wu, Cellular heterogeneity: When do differences make a difference? *Cell* **141**, 559 (2010).
41. I. Dagogo-Jack, A. T. Shaw, Tumour heterogeneity and resistance to cancer therapies. *Nat. Rev. Clin. Oncol.* **15**, 81–94 (2017).
42. N. A. Syed, A. Bhatti, S. Ahmed, H. Syed, P. John, "Single-cell omics in metabolic disorders" in single-cell omics: Volume 2" in *Application in Biomedicine and Agriculture*, D. Barh, V. Azevedo, Eds. (Elsevier, Inc., 2019) pp. 153–164, 10.1016/B978-0-12-817532-3.00008-6.
43. J. Fu *et al.*, Single-cell RNA profiling of glomerular cells shows dynamic changes in experimental diabetic kidney disease. *J. Am. Soc. Nephrol.* **30**, 533–545 (2019).
44. M. V. Holmes *et al.*, Integrating genomics with biomarkers and therapeutic targets to invigorate cardiovascular drug development. *Nat. Rev. Cardiol.* **18**, 435–453 (2021).
45. G. Wallstrom, K. S. Anderson, J. Labaer, Biomarker discovery for heterogeneous diseases. *Cancer Epidemiol. Biomarkers Prev.* **22**, 747–755 (2013).
46. A. Motterle *et al.*, Functional analyses of coronary artery disease associated variation on chromosome 9p21 in vascular smooth muscle cells. *Hum. Mol. Genet.* **21**, 4021–4029 (2012).
47. P. Beri *et al.*, Cell adhesiveness serves as a biophysical marker for metastatic potential. *Cancer Res.* **80**, 901–911 (2020), 10.1158/0008-5472.CAN-19-1794.
48. G. E. Hivchia *et al.*, A novel microfluidic platform for size and deformability based separation and the subsequent molecular characterization of viable circulating tumor cells. *Int. J. Cancer* **138**, 2894–2904 (2016).
49. S. Ribeiro-Samy, Fast and efficient microfluidic cell filter for isolation of circulating tumor cells from unprocessed whole blood of colorectal cancer patients. *Sci. Rep.* **9**, 1–12 (2019).
50. X. Han *et al.*, Microfluidic cell deformability assay for rapid and efficient kinase screening with the CRISPR-Cas9 system. *Angew. Chem. Int. Ed. Engl.* **55**, 8561–8565 (2016).
51. Z. Chen, X. Luo, X. Zhao, M. Yang, C. Wen, Label-free cell sorting strategies via biophysical and biochemical gradients. *J. Orthop. Transl.* **17**, 55 (2019).
52. Y. Ai, P. Li, Label-free multivariate biophysical phenotyping-activated acoustic sorting at the single-cell level. *Anal. Chem.* **93**, 4108–4117 (2021).
53. V. Volpato, C. Webber, Addressing variability in iPSC-derived models of human disease: Guidelines to promote reproducibility. *Dis. Model Mech.* **13**, dmm042317 (2020).
54. N. Paddillaya *et al.*, Biophysics of cell-substrate interactions under shear. *Front. Cell Dev. Biol.* **7**, 251 (2019).
55. Z. Zhao, Individualized lncRNA differential expression profile reveals heterogeneity of breast cancer. *Oncogene* **40**, 4604–4614 (2021).
56. Y. L. Liang, A lncRNA signature associated with tumor immune heterogeneity predicts distant metastasis in locoregionally advanced nasopharyngeal carcinoma. *Nat. Commun.* **13**, 1–12 (2022).
57. K. Jandl *et al.*, Long non-coding RNAs influence the transcriptome in pulmonary arterial hypertension: The role of PAXIP1-AS1. *J. Pathol.* **247**, 357–370 (2019).
58. V. Simion *et al.*, lncRNA VINAS regulates atherosclerosis by modulating NF- $\kappa$ B and MAPK signaling. *JCI Insight* **5**, e140627 (2020).
59. H. Cho *et al.*, Splice variants of lncRNA RNA ANRIL exert opposing effects on endothelial cell activities associated with coronary artery disease. *RNA Biol.* **17**, 1391–1401 (2020).
60. A. Banisadr *et al.*, EGFRvIII uses intrinsic and extrinsic mechanisms to reduce glioma adhesion and increase migration. *J. Cell Sci.* **133**, jcs247189 (2020).
61. K. Baldwin, A. Torkamani, V. Lo Sardo, P. Chubukov, Unveiling the role of the most impactful cardiovascular risk locus through haplotype editing at cell. NCBI Gene Expression Omnibus. <https://www.ncbi.nlm.nih.gov/geo/query/acc.cgi?acc=GSE120099>. Deposited 18 September 2018.
62. J. Mayner *et al.*, Heterogeneous expression of alternatively spliced lncRNA mediates vascular smooth cell plasticity. NCBI Gene Expression Omnibus. <https://www.ncbi.nlm.nih.gov/geo/query/acc.cgi?acc=GSE211144>. Deposited 12 August 2022.